ACS Energy LETTERS

http://pubs.acs.org/journal/aelccp

Degradation by Kinking in Layered Cathode Materials

Yanshuai Li,[▽] Xiaomei Li,[▽] Congcong Du, Haiming Sun, Yin Zhang, Qiunan Liu, Tingting Yang, Jun Zhao, Claude Delmas, Stephen J. Harris, Hailong Chen, Qiao Huang, Yongfu Tang,* Liqiang Zhang,* Ting Zhu,* and Jianyu Huang*

Cite This: *ACS Energy Lett.* 2021, 6, 3960−3969

Read Online

ACCESS | Metrics & More | Article Recommendations | Supporting Information

ABSTRACT: **Layered cathode materials are commonly used in lithium and sodium ion batteries, but they are prone to degradation under electrochemical cycling during battery operation. Here we report a new type of degradation mechanism through the electrochemically induced mechanical buckling and delamination cracking of intercalation layers in a P2 $Na_{0.7}$-$Ni_{0.3}Mn_{0.6}Co_{0.1}O_2$ (Na-NMC) cathode material. Kinks form in the delaminated layers due to severe local bending, and each kink consists of a vertical array of dislocations, resulting from an easy slip between transition metal oxide layers. *In situ* mechanical compression experiments directly reveal the kink formation due to strong mechanical anisotropy parallel and perpendicular to the intercalation layers in single-crystal Na-NMC. *In situ* electrochemical experiments indicate that kinks form during the desodiation process. Our results unveil a new mechanism of electrochemically induced mechanical degradation stemming from weak interlayer bonding in layered cathode materials. This work has broad implications for the mitigation of degradation associated with irreversible interlayer slip in layered cathode materials.**

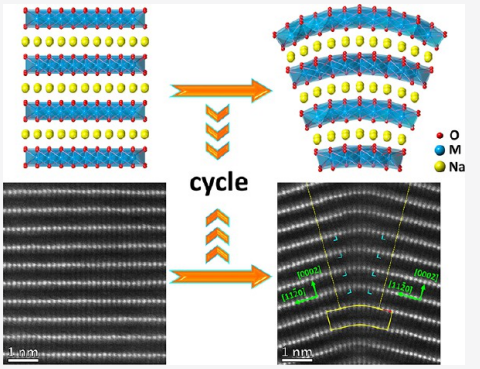

Layered cathode materials such as Li/Na-NMC (Li/Na-$Ni_xMn_yCo_{1-x-y}O_2$) possess high specific capacity for lithium or sodium ion batteries (LIBs or SIBs) in electric vehicle and grid storage applications.[1−10] However, electrochemical cycling of Li/Na-NMC cathodes often results in the accumulation of extended defects such as dislocations[11−16] and cracks[17−24] and the kinetic hindrance of sodiation/desodiation induced by formation of cathode−electrolyte interphases (CEIs),[25,26] leading to capacity fade, short cycle life, and premature failure of batteries.[27−30] Understanding these degradation mechanisms is critical to improving the performance of LIBs and SIBs. Significant progress has been achieved toward understanding defect structures and phase transformations in Li/Na-NMC by high-resolution transmission electron microscopy (HRTEM). For example, intragranular cracking and dislocation formation in a single-crystalline Li-NMC cathode after cycling were observed to understand the origin of capacity fade of LIBs.[22] Recently, Bi et al.[31] found reversible sliding and microcracking along the (003) plane in a single-crystalline Ni-rich Li-NMC cathode, providing clues to mitigate particle fracture from synthesis modification. Despite these advances, the degradation mechanisms associated with electrochemically induced irreversible plastic deformation in layered cathode materials are still not well understood.

The structure of layered cathode materials of the AMO_2 (A = alkali metal, M = transition metal, and O = oxygen) type comprises MO_2 layers of edge-sharing MO_6 octahedra, and each MO_6 octahedron consists of six O atoms occupying the vertices and one transition-metal atom residing at the center. Between the MO_2 layers, alkali-metal ions occupy either octahedral or trigonal-prismatic sites. Figure 1a presents a typical layered $NaMO_2$ structure with sodium ions in prismatic sites. Bonding interactions within the MO_2 layers are generally much stronger than those between the layers. In two-dimensional (2D) van der Waals crystals such as few-layer graphene, MoS_2, and WSe_2, weak bonding interactions within van der Waals gaps allow an easy interlayer slip, thereby facilitating plastic bending, delamination cracking, and kink formation.[32−37] Similar deformation modes could arise in layered cathode materials but have not been well studied.

Received: September 13, 2021
Accepted: October 19, 2021
Published: October 21, 2021

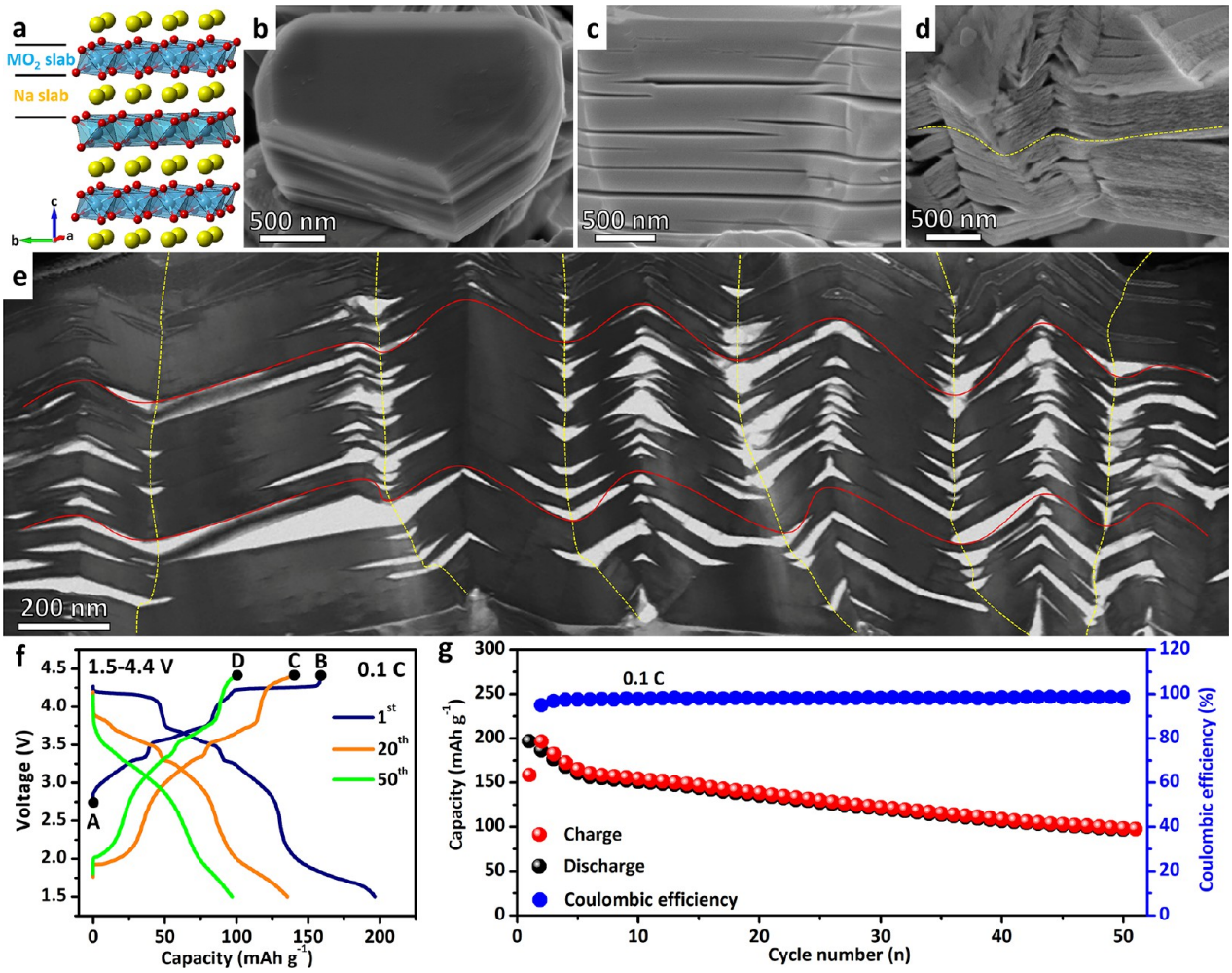

Figure 1. Kink formation in Na-NMC after cycling. (a) Structure model of P2 Na-NMC. (b) SEM image of a single-crystal Na-NMC. The layered structure is apparent at the crystal edge. (c−e) Na-NMC after cycling, showing delamination along basal planes and formation of kinks. The kink density and kink angle increase with cycles. After the 1st charge (desodiation), numerous delamination cracks nearly parallel to basal planes emerged (c). Small bending of basal planes is also visible. After 50 cycles, wavy layers emerged (d, e). (e) Cross-section view of the kinks in the delaminated layers with wavy shape. The sample conditions are (b) pristine, (c) 1st charge to 4.4 V, (d), 20th charge to 4.4 V, and (e) 50th charge to 4.4 V, which correspond to points A−D in (f), respectively. (f) Charge−discharge curves of $Na_{0.7}$-$Ni_{0.3}Mn_{0.6}Co_{0.1}O_2$. (g) Cycling performance of $Na_{0.7}$-$Ni_{0.3}Mn_{0.6}Co_{0.1}O_2$ at 0.1C.

Here we report a degradation mechanism through electrochemically induced irreversible plastic deformation in Na-NMC after electrochemical cycling. We observed buckled MO_2 layers containing a number of sharp kinks interlaced with delamination cracks along the basal planes of Na-NMC. *In situ* compression of Na-NMC single crystals produced similar kink structures. Furthermore, we show that the compressive strength perpendicular to the basal plane of the transition-metal oxide layers is more than 2 times higher than that parallel to the basal plane, indicative of a strong mechanical anisotropy in Na-NMC that gives rise to the formation of multiple kinks. *In situ* electrochemical cycling indicates that kinks and delamination cracks form during desodiation. On the basis of these results, we discuss broader implications of degradation associated with weak interlayer bonding and irreversible slip in layered materials.

According to Delmas' notation,[38] the layered structures are designated as O1, O2, O3 and P1, P2, P3. Here O and P represent the octahedral and prismatic coordinations of an alkali metal between the MO_2 layers, respectively, and 1, 2, and 3 indicate the number of MO_2 layers in the repeating unit. During electrochemical cycling, alkali metal ions are inserted and extracted between the MO_2 layers, while these layers keep their own structure intact. Because Na^+ ions are much larger than Li^+ ions, the interlayer spacing in Na-NMC is larger than that of Li-NMC, thus weakening the interlayer bonding in Na-NMC. As such, the transition metal oxide layers can much more easily glide in Na-NMC than in Li-NMC, producing a variety of phases in the Na-NMC cathodes.[15,39−41]

The pristine phase of $Na_{0.7}$-$Ni_{0.3}Mn_{0.6}Co_{0.1}O_2$ in this work exhibits the P2 structure (Figures S1 and S2a−c) (a = 2.877 Å, c = 11.173 Å, space group $P6_3/mmc$) with a layered morphology (Figure 1b and Figures S2c and S3a). The Na-NMC samples were galvanostatically cycled at a low rate (C/10) between 1.5 and 4.4 V using a coin cell with a Na anode. The charge−discharge curves are shown in Figure 1f. The specific capacity was 196.6 mAh g^{-1} at the initial discharge, which decayed with increasing cycles (Figure 1f,g). Such a capacity decay may be related to structural degradation,[42] phase transformation,[43,44] surface reconstruction,[45,46] or incomplete and kinetically hindered discharge[47,48] of the Na-NMC cathode. To understand degradation mechanisms, we

https://doi.org/10.1021/acsenergylett.1c01976
ACS Energy Lett. 2021, 6, 3960−3969

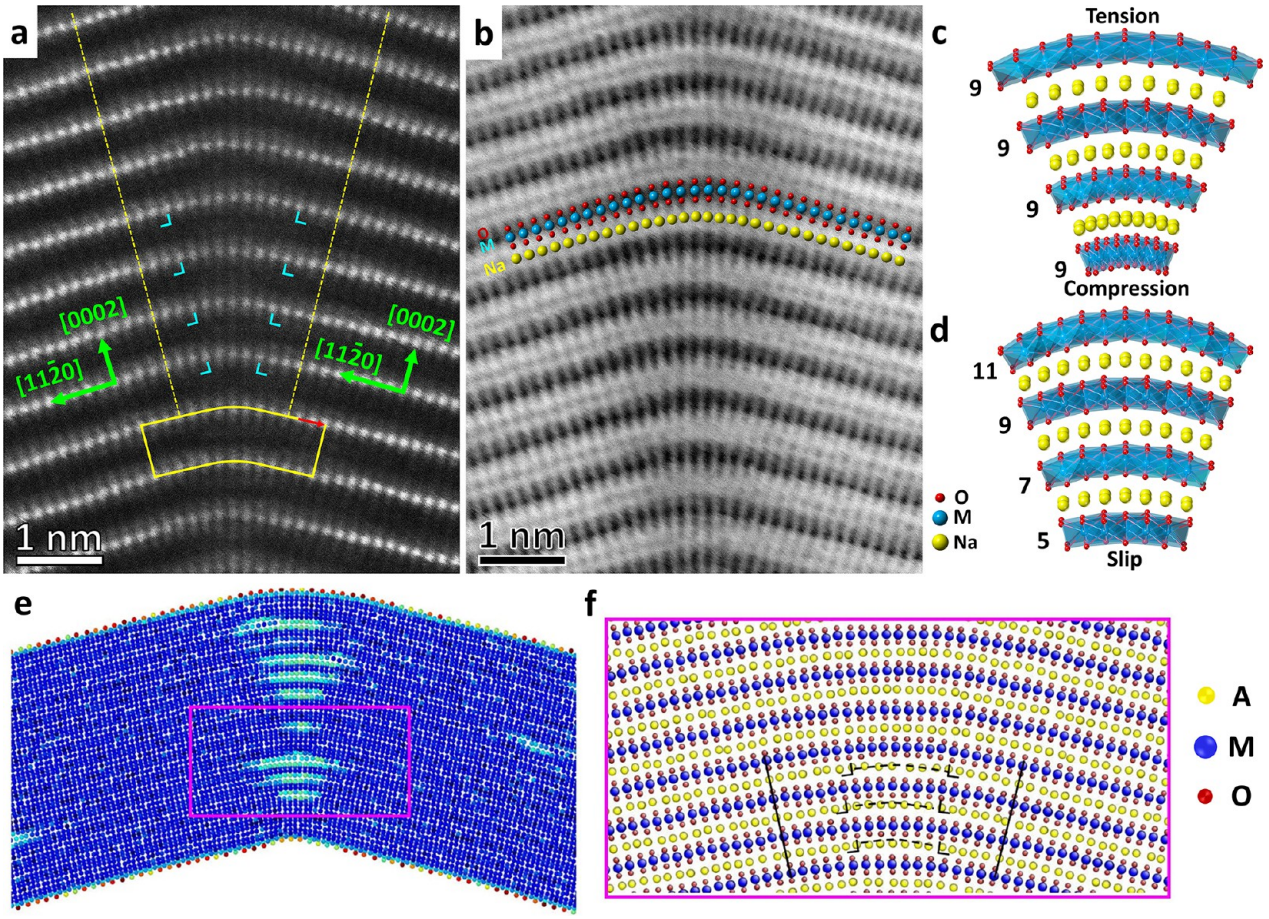

Figure 2. Atomic structure of a kink formed in Na-NMC after cycling. (a) HAADF image viewed along the $[1\bar{1}0]$ direction, showing the kinked MO_2 layers. Large white dots correspond to transition metal ions. The kinked region (delimited by the two yellow dashed lines) consists of an array of dislocations stacked vertically one above another. A Burgers circuit analysis by yellow solid lines gives an unclosed circuit indicated by a red arrow, representing the Burgers vector of $1/3[\bar{1}\bar{1}20]$ for a full dislocation in a MO_2 layer. Each full dislocation is dissociated into two partial dislocations as marked by the symbols ⌋ and ⌊; the two partial dislocations are evidenced by a change of two atomic columns of transition metal ions between two adjacent MO_2 layers. (b) ABF image corresponding to (a), directly showing Na ions between MO_2 layers. (c, d) Structural model of the bending by in-plane tensile/compressive strain of MO_2 layers (c) or interlayer slip (d). (e) MD image showing a kinked region containing an array of vertically aligned dislocations in a model AMO_2 system of $LiCoO_2$. Atoms are colored by central symmetry parameters, such that a short segment of light blue atoms corresponds to a stacking fault in the core of a dissociated dislocation: i.e., between the leading and trailing partials. (f) Atomic structure in the kinked region, shown by a magnified MD image corresponding to the pink box region in (e). Similar to the case for (a), a full dislocation in a MO_2 layer is dissociated into two partial dislocations as marked by the symbols ⌋ and ⌊; the two partial dislocations are evidenced by a change of two atomic columns of transition metal ions between two adjacent MO_2 layers.

conducted a microstructure characterization of the Na-NMC samples under various cycling conditions, marked as A−D in the charge−discharge curves in Figure 1f. After cycling, delamination cracks and kinks emerged (Figure 1c−e and Figures S2d,e and S3b−d). Scanning electron microscopy (SEM) images of a cycled Na-NMC single crystal show the severely bent layered structures containing a number of delamination cracks along the basal planes and sharp kinks in the delaminated layers (Figure 1d,e and Figures S2d,e and S3b−d), indicative of the occurrence of compression-induced buckling instability and resultant large plastic deformation in the layered structures of Na-NMC during cycling. The kinked layers exhibit a wavy shape with the amplitude varying from ∼90 to ∼120 nm and the wavelength ranging from ∼390 to ∼470 nm (Figure 1e). Such kinds of kinked structures are not observed in the pristine Na-NMC samples and thus are the result of large mechanical compression induced by electrochemical cycling. Since the kinked layers and delamination cracks are mostly along the basal planes of the Na-NMC crystal, it can be inferred that there is a strong anisotropy of the mechanical properties between the crystallographic directions perpendicular and parallel to the basal plane of Na-NMC. Incidentally, kinks and delamination cracks have been frequently observed in layered materials such as graphite[31,33,35] and hexagonal boron nitride[33,34] with weak interlayer atomic bonding. For each kink in Figure 1e, the axis of bending rotation of the MO_2 layers is along the out-of-plane $[1\bar{1}0]$ direction, and each $(11\bar{2}0)$ kink plane bisects the bending angle of MO_2 layers (indicated by a yellow dashed line). The density of kinks along the delaminated layers in Na-NMC crystals increased with cycles (Figure 1c−e and Figure S3). To investigate the possible size effect on crack formation, we examined a number of Na-NMC particles after 50 cycles. The initial particle size varies from 1 to 6 μm. After 50 cycles, cracks were observed in almost all of the particles (Figure S4a−d) regardless of their initial sizes. However, there are some subtle

https://doi.org/10.1021/acsenergylett.1c01976
ACS Energy Lett. 2021, 6, 3960−3969

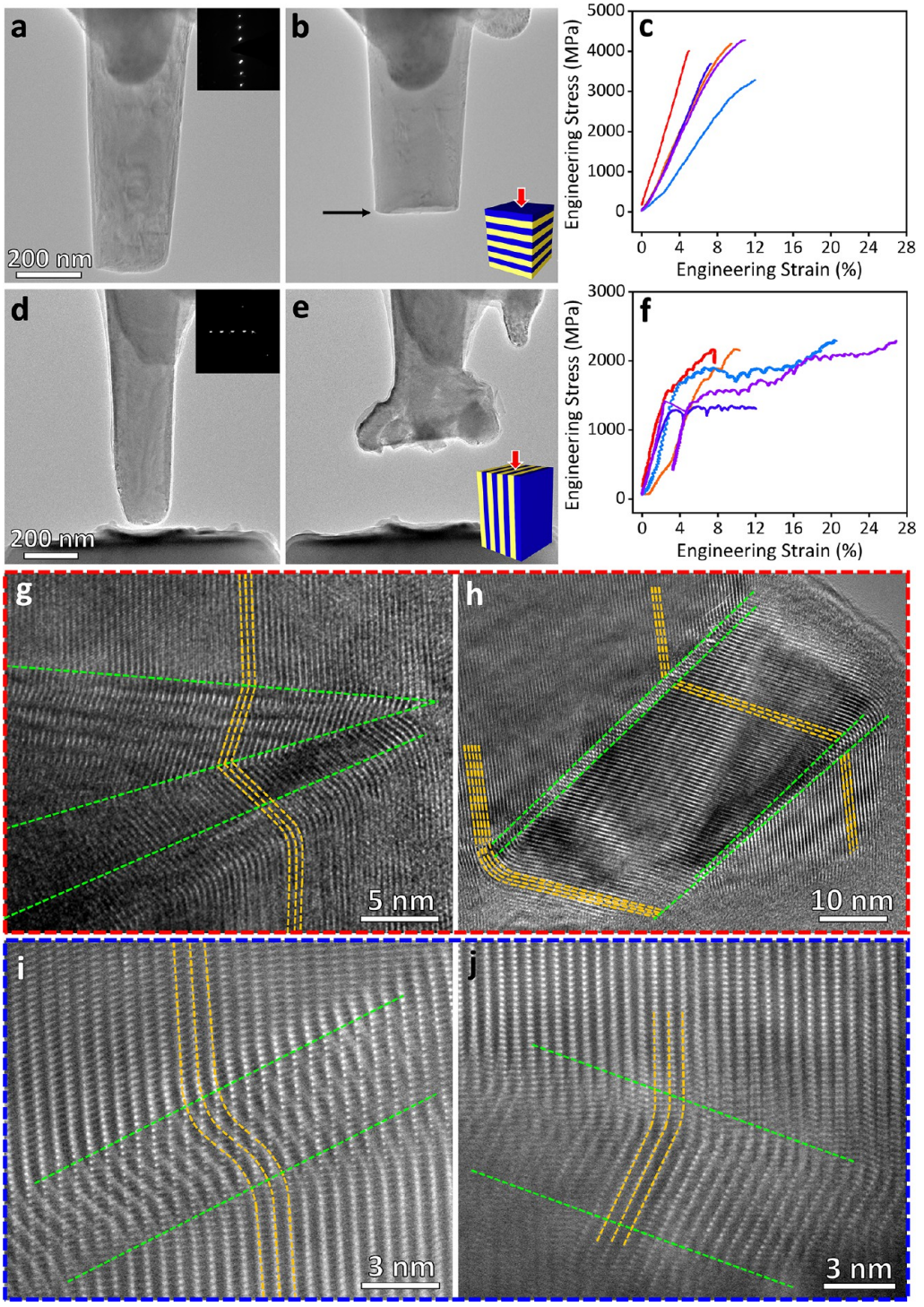

Figure 3. ***In situ*** **compression of single-crystalline Na-NMC pillars. (a, b) Compression along the direction perpendicular to the basal plane. (a) and (b) are TEM images before and after compression, respectively. Note the formation of a brittle fracture surface (indicated by an arrow) in the pillar after compression (b). (c) Stress−strain plots for compression of pillars perpendicular to the basal plane. (d, e) Compression along the direction parallel to the basal plane. (d) and (e) are TEM images before and after compression, respectively. Note the large lateral extension near the compressed surface of the pillar as well as the splitting cracks in the pillar after compression (e), indicating a ductile response for compression along the basal plane. (f) Stress−strain plots for compression of pillars parallel to the basal plane. HRTEM (g, h) and HAADF (i, j) images showing kink formation after compression. In (i) and (j), only parts of the crystalline planes have kinked, whose lattice fringes overlap that of the nonkinked part, forming Moire fringes in the overlapped regions (marked by green dashed lines).**

differences in the morphology and density of the cracks. Namely, some cracks are wavy (Figure S4a,b), while others exhibit kinking (Figure S4c,d), the crack density varies from particle to particle, and no size effect on crack formation can be clearly identified. Therefore, in the particle size range from 1 to 6 μm, no size effect was observed. However, this study does

https://doi.org/10.1021/acsenergylett.1c01976
ACS Energy Lett. 2021, 6, 3960−3969

not rule out the possibility of a size effect in a wider particle size distribution from a few nanometers to a few hundred micrometers, which warrants further study in the future.

The atomic structure of individual kinks is revealed by scanning transmission electron microscopy (STEM) imaging. The STEM high angle annular dark field (HAADF) image in Figure 2a shows a narrowly kinked region that spans less than 10 interconnected MO_6 octahedra in each MO_2 layer. A large bending angle of ~30° (Figure S5) forms across the kink, and it is achieved through continuous rotation of MO_6 octahedra. The two sides of the kink are almost symmetrical with respect to the central kink plane of $(11\bar{2}0)$. The STEM annular bright field (ABF) image in Figure 2b shows the arrangement of Na^+ ions between adjacent MO_2 layers (indicated by yellow dots in Figure 2b). Apparently, the bending deformation does not alter the arrangement of intercalation sites of Na^+ ions: namely, each Na^+ ion layer is bent with its adjacent MO_2 layers across the kink.

In general, bending has to be accommodated by either in-plane strain of MO_2 layers (Figure 2c) or interlayer slip (Figure 2d). These two competing modes of bending deformation can be distinguished by comparing the number of MO_6 octahedra across the bent MO_2 layers, which remains constant in the case of in-plane strain but increases in the case of interlayer slip. We compare the model structures from these two bending modes (Figures 2c,d) with the kinked structure in the HAADF image (Figure 2a). In the largely bent region (delimited by the two yellow dashed lines) in Figure 2a, the number of atomic columns of transition metal ions and thus the number of MO_6 octahedra changes by 2 between two adjacent MO_2 layers. In contrast, outside the bent region, the MO_2 layers are flat; the atomic columns of transition metal ions and thus the MO_6 octahedra are perfectly aligned and their numbers remain identical in all of the MO_2 layers. Hence, interlayer slip has occurred in the kinked region. A Burgers circuit analysis in Figure 2a indicates that the Burgers vector is $1/3[\bar{1}\bar{1}20]$, which is a full dislocation in the basal plane of a hexagonal crystal. It appears that the perfect dislocation is dissociated into two partial dislocations according to $1/3[\bar{1}\bar{1}20] \rightarrow 1/3[\bar{1}010] + 1/3[0\bar{1}\bar{1}0]$, which give rise to a change of the number of atomic columns of transition metal ions and thus the number of MO_6 octahedra by 2 between two adjacent MO_2 layers. As such, the bending deformation associated with the kink is accommodated by two partial dislocation walls (marked respectively by the symbols ⌋ and ⌊), each of which consists of a vertical array of partial dislocations at each side of the kink, and each dislocation wall is perpendicular to the local basal plane (Figure 2a).

Interlayer slip is an important microscopic mechanism of plastic deformation and degradation in layered cathode materials. On the basis of the above experimental observations, we performed molecular dynamics (MD) simulations to analyze the dislocations resulting from bending-induced interlayer slip in layered oxides. Figure 2e,f show the representative MD results of formation of a sharp kink consisting of a vertical array of dislocations in a model AMO_2 system of $LiCoO_2$, which are consistent with the HAADF images in Figure 2a,b. More specifically, bending was imposed on a $LiCoO_2$ slab (Figure S6a) with weak bonding between MO_2 layers. Initially, the MO_2 layers experienced an elastic bending deformation (Figure S6b and Movie S1). Increased bending caused the formation of a sharp kink, where a slip between the MO_2 layers produced dislocations (Figure S6c and Movie S1). Further bending led to an increase of the kink angle, with an increasing number of dislocations in the kinked region (Figure S6d and Movie S1). Figure S6e shows the simulated HAADF image of a kinked region in Figure 2e,f and Figure S6d containing several dislocations, while Figure 2f and Figure S6f show the corresponding atomic structure containing the alkali metal layer between the MO_2 layers.

We note that, for a dislocation core between two adjacent MO_2 layers in Figures 2e,f and Figure S6d, there are two extra atomic columns of transition metal ions (Figure 2f) and thus two extra MO_6 octahedra in the top MO_2 layer, consistent with the experimental HAADF and ABF images in Figure 2a,b, respectively. Close examination of the three-dimensional atomic structure from MD confirms that the two extra atomic columns in a MO_2 layer correspond to the respective core of a leading and a trailing partial (indicated respectively by the symbols ⌋ and ⌊ in Figure 2f) of a full dislocation, with a stacking fault (indicated by short dashed lines in Figure 2f and Figure S6e) between the two partial dislocations. As such, the kink consists of an array of full dislocations (equivalent to two arrays of partial dislocations) stacked vertically one above another, which effectively forms a symmetrical tilt grain boundary (GB). For such kind of GB, the geometrical relation of $2D \sin(\theta/2) = b$ holds, where D is the spacing between the dislocations, b is the Burgers vector length, and θ is the GB angle (i.e., misorientation across a GB). In the GB shown Figure 2a, every MO_2 layer contains a full dislocation, such that D takes the smallest limit of the spacing between two adjacent MO_2 layers. Using the above geometrical relation along with the measured values of b = 2.877 Å and D = 5.59 Å, we estimated θ = 29.8°, which agrees with the measured value of 30° from the STEM images in Figure 2a.

We obtained similar MD results of bending-induced kinks and dislocations stemming from interlayer slip in another AMO_2 model system of $LiNi_{1/3}Mn_{1/3}Co_{1/3}O_2$ with weak bonding between MO_2 layers (Figure S7 and Movie S2). While there is currently a lack of robust interatomic potentials for simulation of the Na-based AMO_2 systems, our MD results from the two Li-based AMO_2 model systems provide atomic-level insights into the irreversible interlayer slip and resulting dislocation structures in layered cathode materials with weak interlayer bonding. Future studies are needed to evaluate the effect of the octahedral versus trigonal-prismatic coordination of alkali metal ions on the interlayer slip, after reliable interatomic potentials become available for the Na-based AMO_2 systems.

The large bending of the MO_2 layers through an interlayer slip suggests weaker interlayer bonding in comparison to intralayer bonding, indicating the mechanical anisotropy of Na-NMC crystals. To test this hypothesis, we conducted *in situ* mechanical compression experiments of Na-NMC single crystals with an applied load either perpendicular or parallel to the basal plane. Figure 3a,b and Movie S3 show compression perpendicular to the basal plane. The initial single-crystalline Na-NMC pillar (Figure 3a) appeared to withstand little plastic deformation, and it fractured with a sharp fracture surface (indicated by a black arrow in Figure 3b and Movie S3) parallel to the basal plane after compression. The corresponding stress−strain curve deviates slightly from the initial linear response beyond the elastic limit (Figure 3c), which is consistent with the brittle fracture observed by TEM (Figure 3a,b). The average yield strength (defined as the stress at the elastic limit in the stress−strain curve) is about 3.68 GPa

https://doi.org/10.1021/acsenergylett.1c01976
ACS Energy Lett. 2021, 6, 3960−3969

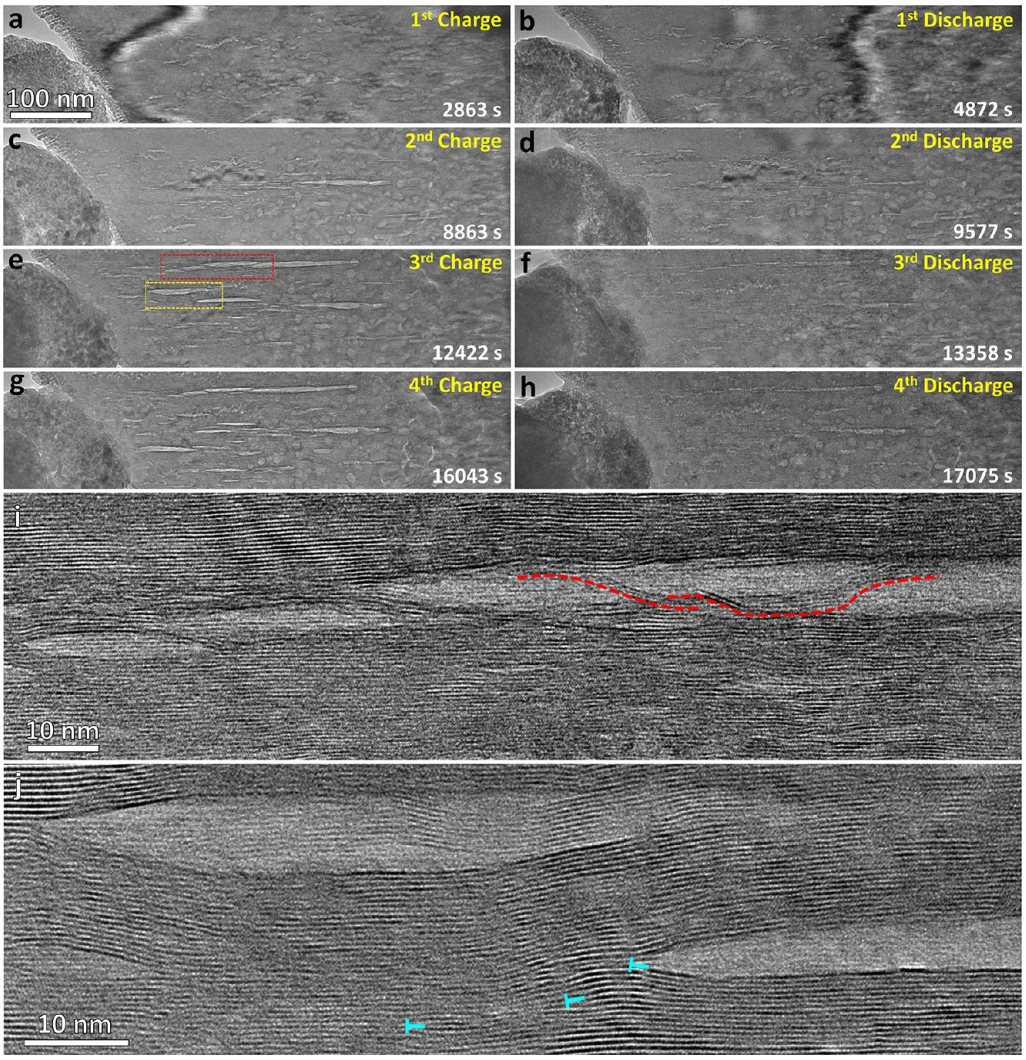

Figure 4. ***In situ*** **TEM images showing structural evolution during four charge−discharge cycles of the Na-NMC cathode. Note that microcracks are readily visible after the first desodiation (a), and the population, length, and width of the cracks increase with increasing number of desodiation (a, c, e, g). The cracks appear to be mostly closed after each sodiation (b, d, f, h). (i, j) HRTEM images of the cracks and delaminated layers formed during the third desodiation. (i) and (j) are local magnification from the red and yellow boxed regions in (e), respectively. Symbols ⊥ in (j) mark dislocations.**

(Table S1). In contrast, compression along the basal plane resulted in substantial plastic deformation (Figure 3d,e and Movie S4); the compressed pillar (Figure 3e) became shortened, while it extended along the lateral direction. The pillar split into several small columns with bent layers and kinks (Figure 3e,g−j and Figure S8). The stress−strain curves from this loading orientation (Figure 3f) exhibit extensive nonlinear responses with large plastic strain limits ranging from ∼8% to 28%. The average yield strength along the basal plane is about 1.57 GPa (Table S1), which is more than 2 times smaller than that from compression vertical to the basal plane (3.68 GPa). These results demonstrate the strong mechanical anisotropy of the Na-NMC crystals. Notably, HRTEM and HAADF images of the deformed samples indicate that bending and kinking are the dominant mechanisms of plastic deformation (Figure 3g−j and Figure S8). Kinks similar to those formed in the electrochemically cycled samples were also observed in the Na-NMC samples mechanically deformed along the basal plane (Figure 3g−j and Figure S8). These results indicate that mechanical anisotropy is the intrinsic property of layered cathode materials. Weak interlayer bonding leads to an interlayer slip. A localized and nonuniform interlayer slip results in the formation of kinks, in contrast to a delocalized and uniform interlayer slip giving rise to a phase transformation in layered Na-NMC cathodes. From *in situ* compression experiments, the average yield strength parallel to the basal plane is about 1.57 GPa and kinks form near the yield strength. The observation of a large amount of kinks in Na-NMC suggests that the local mechanical stress generated during electrochemical processes is in the range of 1.57 GPa, which agrees well with the stress generation in anode materials.[49,50]

Although interlayer cracks have been observed in Na-NMC after electrochemical cycling, it is unclear whether they form during sodiation or desodiation, and the same question also arises regarding the formation of kinks. To address these questions, we conducted *in situ* electrochemical cycling of a Na-NMC cathode (Figure 4, Figure S9 and Movie S5). Delamination cracks emerged and opened up even during the first desodiation (Figure 4a). With increasing cycles, the length and width of the cracks increased gradually (Figure 4c,e). We found that such wide cracks were not formed immediately

https://doi.org/10.1021/acsenergylett.1c01976
ACS Energy Lett. 2021, 6, 3960−3969

upon cycling but resulted from cumulative growth over many cycles (Figure 4g). We verified that the cracks are not caused by electron beam irradiation (Figure S10). The opening cracks observed after desodiation were closed after each sodiation process (Figure 4b,d,f,h). As the cracks grew longer, some delaminated layers were largely bent, bridging two adjacent opening cracks (Figure 4i,j). Delaminated layers were also formed and bent to connect the top and bottom surfaces of the same opening crack (Figure 4i,j). With increasing cycles, the bending deformation of delaminated layers increased. These *in situ* results indicate that the formation of delaminated layers and the associated large bending and kinking of these layers occurred during the desodiation processes. To explore the effect of sample thickness on the cracking behavior of Na-NMC, we built a nanobattery with the coexisting thin and thick areas of Na-NMC for *in situ* TEM experiments (Figure S11a). As shown in Figure S11b,c, the thickness of the thin area of Na-NMC is about 200 nm, while that of the thick area is about 2 μm. After the third charge, cracks emerged not only in the thin area but also in the thick area (marked by a yellow arrow in Figure S11d). This result indicates that the sample thickness has a negligible effect on crack formation in the range studied in this work.

During desodiation, the lattice parameter along the *a* axis in the basal plane decreases, while that along the *c* axis perpendicular to the basal plane increases; during sodiation, the change in lattice parameter along the *a* axis and *c* axis is reversed.[19,43,44] Indeed, we measured the lattice parameters of pristine Na-NMC of and Na-NMC after the first charge and discharge, which show that *c* = 5.66, 5.90, and 5.55 Å, respectively, while the change in *a* is indiscernible (Figure S12 and Table S2). These results indicate that the first desodiation and sodiation generate a tensile strain of ∼4.2% and a compressive strain of 5.9% along the *c* axis, respectively, consistent with previous measurements in P2 structures.[44] Desodiation usually starts from surfaces, leading to concentration gradients that induce nonuniform lattice deformations (Figure S13a,b). Upon cell charge, the increase of the *c* parameter of the external part of a single-crystalline particle causes tension of the internal part along the *c* direction, which can induce the formation of delamination cracks along the basal planes. On the other hand, the decrease in the *a* parameter of the external part of the particle causes compression of the internal part along the *a* direction, which can induce the bending and kinking of delaminated layers (Figure S13c,d). Cycling of Na-NMC introduces an increasing amount of defects such as dislocations, delamination cracks, and kinks. These defects in turn cause nonuniform sodium extraction and insertion, which promote the formation of defects. These processes lead to cumulative degradation of Na-NMC electrodes with increasing cycles.

To summarize, kinking is an essential mode of plastic deformation in layered materials with weak interlayer bonding. A kinked region exhibits an abrupt orientation change around the kink plane.[51] Our results show that in Na-NMC, the kink plane is $\{11\bar{2}0\}$, the rotation axis in the kink plane is $\langle 1\bar{1}00\rangle$, and the kink angle is up to ∼40°. During the kinking process, an interlayer slip occurs to accommodate the large bending deformation of MO_2 layers and is presumably facilitated by the decreased amount of Na^+ ions between MO_2 layers during desodiation. In contrast to the previous studies of interlayer slip giving rise to phase transformation,[15,52] our work reveals the localized and nonuniform interlayer slip between MO_2 layers resulting in kink formation. In fact, a kink consists of an array of dislocations stacked vertically one above another. Each dislocation in this array dissociates into the leading and trailing partial dislocations, giving a narrowly kinked region spanning less than 10 interconnected MO_6 octahedra in each MO_2 layer. Kinking in Na-NMC results from severe local bending of delaminated layers and thus represents a unique mechanism of electrochemically induced mechanical degradation stemming from weak interlayer bonding in layered cathode materials. An increasing amount of kinks with electrochemical cycling reflects the accumulation of irreversible, localized interlayer slips in Na-NMC. A further in-depth study of the interlayer slip and resulting kinking phenomena is essential to finding effective means of mitigating the degradation in layered cathode materials. Broadly, kinking in layered oxides has the same root cause of weak interlayer bonding as that in 2D van der Waals crystals. Kinks in single-layer or few-layer oxides may exhibit intriguing mechanical and physical properties as 2D van der Waals crystals do.[36,53,54] As such, our study suggests a possibility of making the kinked structures and investigating their properties in 2D materials based on layered oxides for functional applications.

■ ASSOCIATED CONTENT

Supporting Information

The Supporting Information is available free of charge at https://pubs.acs.org/doi/10.1021/acsenergylett.1c01976.

Methods, characterization data and additional figures and tables as described in the text (PDF)

MD movie showing the bending deformation of a LCO slab (MP4)

MD movie showing the bending deformation of a Li-NMC slab (MP4)

In situ TEM movie showing the compression of a Na-NMC pillar along the *c* axis direction (MP4)

In situ TEM movie showing the compression of a Na-NMC pillar along the basal planes (MP4)

In situ TEM movie showing the structural evolution of four cycles of the Na-NMC cathode (MP4)

■ AUTHOR INFORMATION

Corresponding Authors

Yongfu Tang − *Clean Nano Energy Center, State Key Laboratory of Metastable Materials Science and Technology, Yanshan University, Qinhuangdao 066004, People's Republic of China*; orcid.org/0000-0002-6318-3110; Email: tangyongfu@ysu.edu.cn

Liqiang Zhang − *Clean Nano Energy Center, State Key Laboratory of Metastable Materials Science and Technology, Yanshan University, Qinhuangdao 066004, People's Republic of China*; Email: liqiangzhang85@163.com

Ting Zhu − *Woodruff School of Mechanical Engineering, Georgia Institute of Technology, Atlanta, Georgia 30332, United States*; Email: ting.zhu@me.gatech.edu

Jianyu Huang − *Clean Nano Energy Center, State Key Laboratory of Metastable Materials Science and Technology, Yanshan University, Qinhuangdao 066004, People's Republic of China; Key Laboratory of Low Dimensional Materials and Application Technology of Ministry of Education, School of Materials Science and Engineering, Xiangtan University, Xiangtan 411105, China*; orcid.org/0000-0002-8424-5368; Email: jyhuang8@hotmail.com

https://doi.org/10.1021/acsenergylett.1c01976
ACS Energy Lett. 2021, 6, 3960−3969

Authors

Yanshuai Li − *Clean Nano Energy Center, State Key Laboratory of Metastable Materials Science and Technology, Yanshan University, Qinhuangdao 066004, People's Republic of China*

Xiaomei Li − *Clean Nano Energy Center, State Key Laboratory of Metastable Materials Science and Technology, Yanshan University, Qinhuangdao 066004, People's Republic of China*

Congcong Du − *Clean Nano Energy Center, State Key Laboratory of Metastable Materials Science and Technology, Yanshan University, Qinhuangdao 066004, People's Republic of China*

Haiming Sun − *Clean Nano Energy Center, State Key Laboratory of Metastable Materials Science and Technology, Yanshan University, Qinhuangdao 066004, People's Republic of China; Research Center for Ultra-High Voltage Electron Microscopy, Osaka University, Osaka 565-0871 Ibaraki, Japan;* orcid.org/0000-0001-9085-500X

Yin Zhang − *Woodruff School of Mechanical Engineering, Georgia Institute of Technology, Atlanta, Georgia 30332, United States*

Qiunan Liu − *Clean Nano Energy Center, State Key Laboratory of Metastable Materials Science and Technology, Yanshan University, Qinhuangdao 066004, People's Republic of China*

Tingting Yang − *Clean Nano Energy Center, State Key Laboratory of Metastable Materials Science and Technology, Yanshan University, Qinhuangdao 066004, People's Republic of China*

Jun Zhao − *Clean Nano Energy Center, State Key Laboratory of Metastable Materials Science and Technology, Yanshan University, Qinhuangdao 066004, People's Republic of China*

Claude Delmas − *ICMCB-CNRS, Université de Bordeaux, 33608 Pessac Cedex, France*

Stephen J. Harris − *Energy Storage Division, Lawrence Berkeley National Laboratory, Berkeley, California 94720, United States*

Hailong Chen − *Woodruff School of Mechanical Engineering, Georgia Institute of Technology, Atlanta, Georgia 30332, United States;* orcid.org/0000-0001-8283-2860

Qiao Huang − *Key Laboratory of Low Dimensional Materials and Application Technology of Ministry of Education, School of Materials Science and Engineering, Xiangtan University, Xiangtan 411105, China*

Complete contact information is available at: https://pubs.acs.org/10.1021/acsenergylett.1c01976

Author Contributions

[▽]Y.L. and X.L. contributed equally to this paper.

Notes

The authors declare no competing financial interest.

■ ACKNOWLEDGMENTS

This work was financially supported by the National Natural Science Foundation of China (Nos. 52022088, 51971245, 51772262, 21406191, U20A20336, 21935009, 11575154, 51802277, and 52002346), the Fok Ying-Tong Education Foundation of China (No. 171064), Beijing Natural Science Foundation (No. 2202046), the Natural Science Foundation of Hebei Province (Nos. B2020203037 and B2018203297) and Hunan Innovation Team (2018RS3091), the science and technology innovation Program of Hunan Province (2020RC2079), and the Huxiang Young Talents Plan Project of Hunan Province (2021RC3109). Part of this work was supported by the Assistant Secretary for Energy Efficiency and Renewable Energy, Vehicles Technology Office, of the U.S. Department of Energy under Contract No. DEAC02-05CH11231.

■ REFERENCES

(1) Whittingham, M. S. Ultimate Limits to Intercalation Reactions for Lithium Batteries. *Chem. Rev.* **2014**, *114* (23), 11414−11443.

(2) Goodenough, J. B.; Park, K.-S. The Li-Ion Rechargeable Battery: A Perspective. *J. Am. Chem. Soc.* **2013**, *135* (4), 1167−1176.

(3) Ma, C.; Alvarado, J.; Xu, J.; Clément, R. J.; Kodur, M.; Tong, W.; Grey, C. P.; Meng, Y. S. Exploring Oxygen Activity in the High Energy P2-Type $Na_{0.78}Ni_{0.23}Mn_{0.69}O_2$ Cathode Material for Na-Ion Batteries. *J. Am. Chem. Soc.* **2017**, *139* (13), 4835−4845.

(4) Xiang, X.; Zhang, K.; Chen, J. Recent Advances and Prospects of Cathode Materials for Sodium-Ion Batteries. *Adv. Mater.* **2015**, *27* (36), 5343−5364.

(5) Hwang, J.-Y.; Myung, S.-T.; Sun, Y.-K. Sodium-ion batteries: present and future. *Chem. Soc. Rev.* **2017**, *46* (12), 3529−3614.

(6) Billaud, J.; Singh, G.; Armstrong, A. R.; Gonzalo, E.; Roddatis, V.; Armand, M.; Rojo, T.; Bruce, P. G. $Na_{0.67}Mn_{1-x}Mg_xO_2$ ($0 \leq x \leq 0.2$): a high capacity cathode for sodium-ion batteries. *Energy Environ. Sci.* **2014**, *7* (4), 1387−1391.

(7) Li, W.; Erickson, E. M.; Manthiram, A. High-nickel layered oxide cathodes for lithium-based automotive batteries. *Nat. Energy* **2020**, *5* (1), 26−34.

(8) Xiao, Y.; Abbasi, N. M.; Zhu, Y.-F.; Li, S.; Tan, S.-J.; Ling, W.; Peng, L.; Yang, T.; Wang, L.; Guo, X.-D.; Yin, Y.-X.; Zhang, H.; Guo, Y.-G. Layered Oxide Cathodes Promoted by Structure Modulation Technology for Sodium-Ion Batteries. *Adv. Funct. Mater.* **2020**, *30* (30), 2001334.

(9) Su, H.; Jaffer, S.; Yu, H. Transition metal oxides for sodium-ion batteries. *Energy Storage Mater.* **2016**, *5*, 116−131.

(10) Yoshida, J.; Guerin, E.; Arnault, M.; Constantin, C.; Mortemard de Boisse, B.; Carlier, D.; Guignard, M.; Delmas, C. New P2 - $Na_{0.70}Mn_{0.60}Ni_{0.30}Co_{0.10}O_2$Layered Oxide as Electrode Material for Na-Ion Batteries. *J. Electrochem. Soc.* **2014**, *161* (14), A1987−A1991.

(11) Wang, H.; Jang, Y. I.; Huang, B.; Sadoway, D. R.; Chiang, Y. M. TEM Study of Electrochemical Cycling-Induced Damage and Disorder in $LiCoO_2$ Cathodes for Rechargeable Lithium Batteries. *J. Electrochem. Soc.* **1999**, *146* (2), 473−480.

(12) Gabrisch, H.; Yazami, R.; Fultz, B. The Character of Dislocations in $LiCoO_2$. *Electrochem. Solid-State Lett.* **2002**, *5* (6), A111.

(13) Gabrisch, H.; Yazami, R.; Fultz, B. Hexagonal to Cubic Spinel Transformation in Lithiated Cobalt Oxide. *J. Electrochem. Soc.* **2004**, *151* (6), A891.

(14) Singer, A.; Zhang, M.; Hy, S.; Cela, D.; Fang, C.; Wynn, T. A.; Qiu, B.; Xia, Y.; Liu, Z.; Ulvestad, A.; Hua, N.; Wingert, J.; Liu, H.; Sprung, M.; Zozulya, A. V.; Maxey, E.; Harder, R.; Meng, Y. S.; Shpyrko, O. G. Nucleation of dislocations and their dynamics in layered oxide cathode materials during battery charging. *Nat. Energy* **2018**, *3* (8), 641−647.

(15) Radin, M. D.; Hy, S.; Sina, M.; Fang, C.; Liu, H.; Vinckeviciute, J.; Zhang, M.; Whittingham, M. S.; Meng, Y. S.; Van der Ven, A. Narrowing the Gap between Theoretical and Practical Capacities in Li-Ion Layered Oxide Cathode Materials. *Adv. Energy Mater.* **2017**, *7* (20), 1602888.

(16) Ulvestad, A.; Singer, A.; Clark, J.; Cho, H.; Kim, J. W.; Harder, R.; Maser, J.; Meng, Y.; Shpyrko, O. Topological defect dynamics in operando battery nanoparticles. *Science* **2015**, *348* (6241), 1344−1347.

(17) Sun, H.-H.; Manthiram, A. Impact of Microcrack Generation and Surface Degradation on a Nickel-Rich Layered Li-

[$Ni_{0.9}Co_{0.05}Mn_{0.05}$]$O_2$ Cathode for Lithium-Ion Batteries. *Chem. Mater.* **2017**, *29* (19), 8486−8493.
(18) Miller, D. J.; Proff, C.; Wen, J. G.; Abraham, D. P.; Bareño, J. Observation of Microstructural Evolution in Li Battery Cathode Oxide Particles by In Situ Electron Microscopy. *Adv. Energy Mater.* **2013**, *3* (8), 1098−1103.
(19) Lim, J.-M.; Hwang, T.; Kim, D.; Park, M.-S.; Cho, K.; Cho, M. Intrinsic Origins of Crack Generation in Ni-rich $LiNi_{0.8}Co_{0.1}Mn_{0.1}O_2$ Layered Oxide Cathode Material. *Sci. Rep.* **2017**, *7* (1), 39669.
(20) Kim, U.-H.; Park, G.-T.; Son, B.-K.; Nam, G. W.; Liu, J.; Kuo, L.-Y.; Kaghazchi, P.; Yoon, C. S.; Sun, Y.-K. Heuristic solution for achieving long-term cycle stability for Ni-rich layered cathodes at full depth of discharge. *Nat. Energy* **2020**, *5* (11), 860−869.
(21) Kondrakov, A. O.; Schmidt, A.; Xu, J.; Geßwein, H.; Mönig, R.; Hartmann, P.; Sommer, H.; Brezesinski, T.; Janek, J. Anisotropic Lattice Strain and Mechanical Degradation of High- and Low-Nickel NCM Cathode Materials for Li-Ion Batteries. *J. Phys. Chem. C* **2017**, *121* (6), 3286−3294.
(22) Yan, P.; Zheng, J.; Gu, M.; Xiao, J.; Zhang, J.-G.; Wang, C.-M. Intragranular cracking as a critical barrier for high-voltage usage of layer-structured cathode for lithium-ion batteries. *Nat. Commun.* **2017**, *8* (1), 14101.
(23) Liu, Y.; Harlow, J.; Dahn, J. Microstructural Observations of "Single Crystal" Positive Electrode Materials Before and After Long Term Cycling by Cross-section Scanning Electron Microscopy. *J. Electrochem. Soc.* **2020**, *167* (2), 020512.
(24) Klein, S.; Bärmann, P.; Fromm, O.; Borzutzki, K.; Reiter, J.; Fan, Q.; Winter, M.; Placke, T.; Kasnatscheew, J. Prospects and limitations of single-crystal cathode materials to overcome cross-talk phenomena in high-voltage lithium ion cells. *J. Mater. Chem. A* **2021**, *9* (12), 7546−7555.
(25) Zhang, S.; Ma, J.; Hu, Z.; Cui, G.; Chen, L. Identifying and Addressing Critical Challenges of High-Voltage Layered Ternary Oxide Cathode Materials. *Chem. Mater.* **2019**, *31* (16), 6033−6065.
(26) Kasnatscheew, J.; Evertz, M.; Streipert, B.; Wagner, R.; Nowak, S.; Cekic Laskovic, I.; Winter, M. Changing Established Belief on Capacity Fade Mechanisms: Thorough Investigation of Li-$Ni_{1/3}Co_{1/3}Mn_{1/3}O_2$ (NCM111) under High Voltage Conditions. *J. Phys. Chem. C* **2017**, *121* (3), 1521−1529.
(27) Ryu, H.-H.; Park, K.-J.; Yoon, C. S.; Sun, Y.-K. Capacity Fading of Ni-Rich Li[$Ni_xCo_yMn_{1-x-y}$]O_2 ($0.6 \leq x \leq 0.95$) Cathodes for High-Energy-Density Lithium-Ion Batteries: Bulk or Surface Degradation? *Chem. Mater.* **2018**, *30* (3), 1155−1163.
(28) Hu, E.; Wang, X.; Yu, X.; Yang, X.-Q. Probing the Complexities of Structural Changes in Layered Oxide Cathode Materials for Li-Ion Batteries during Fast Charge−Discharge Cycling and Heating. *Acc. Chem. Res.* **2018**, *51* (2), 290−298.
(29) Zheng, S.; Huang, R.; Makimura, Y.; Ukyo, Y.; Fisher, C. A. J.; Hirayama, T.; Ikuhara, Y. Microstructural Changes in Li-$Ni_{0.8}Co_{0.15}Al_{0.05}O_2$ Positive Electrode Material during the First Cycle. *J. Electrochem. Soc.* **2011**, *158* (4), A357.
(30) Koerver, R.; Zhang, W.; de Biasi, L.; Schweidler, S.; Kondrakov, A. O.; Kolling, S.; Brezesinski, T.; Hartmann, P.; Zeier, W. G.; Janek, J. Chemo-mechanical expansion of lithium electrode materials − on the route to mechanically optimized all-solid-state batteries. *Energy Environ. Sci.* **2018**, *11* (8), 2142−2158.
(31) Bi, Y.; Tao, J.; Wu, Y.; Li, L.; Xu, Y.; Hu, E.; Wu, B.; Hu, J.; Wang, C.; Zhang, J.-G.; Qi, Y.; Xiao, J. Reversible planar gliding and microcracking in a single-crystalline Ni-rich cathode. *Science* **2020**, *370* (6522), 1313−1317.
(32) Han, E.; Yu, J.; Annevelink, E.; Son, J.; Kang, D. A.; Watanabe, K.; Taniguchi, T.; Ertekin, E.; Huang, P. Y.; van der Zande, A. M. Ultrasoft slip-mediated bending in few-layer graphene. *Nat. Mater.* **2020**, *19* (3), 305−309.
(33) Rooney, A. P.; Li, Z.; Zhao, W.; Gholinia, A.; Kozikov, A.; Auton, G.; Ding, F.; Gorbachev, R. V.; Young, R. J.; Haigh, S. J. Anomalous twin boundaries in two dimensional materials. *Nat. Commun.* **2018**, *9* (1), 3597.
(34) Huang, J. Y.; Jia, X. B.; Yasuda, H.; Mori, H. Stacking disordering in hexagonal BN induced by shearing under ball milling. *Philos. Mag. Lett.* **1999**, *79* (5), 217−224.
(35) Huang, J. Y. HRTEM and EELS studies of defects structure and amorphous-like graphite induced by ball-milling. *Acta Mater.* **1999**, *47* (6), 1801−1808.
(36) Nikiforov, I.; Tang, D.-M.; Wei, X.; Dumitrică, T.; Golberg, D. Nanoscale Bending of Multilayered Boron Nitride and Graphene Ribbons: Experiment and Objective Molecular Dynamics Calculations. *Phys. Rev. Lett.* **2012**, *109* (2), 025504.
(37) Tang, D.-M.; Kvashnin, D. G.; Najmaei, S.; Bando, Y.; Kimoto, K.; Koskinen, P.; Ajayan, P. M.; Yakobson, B. I.; Sorokin, P. B.; Lou, J.; Golberg, D. Nanomechanical cleavage of molybdenum disulphide atomic layers. *Nat. Commun.* **2014**, *5* (1), 3631.
(38) Delmas, C.; Fouassier, C.; Hagenmuller, P. Structural classification and properties of the layered oxides. *Physica B+C* **1980**, *99* (1-4), 81−85.
(39) Sun, Y.; Guo, S.; Zhou, H. Adverse effects of interlayer-gliding in layered transition-metal oxides on electrochemical sodium-ion storage. *Energy Environ. Sci.* **2019**, *12* (3), 825−840.
(40) Radin, M. D.; Alvarado, J.; Meng, Y. S.; Van der Ven, A. Role of Crystal Symmetry in the Reversibility of Stacking-Sequence Changes in Layered Intercalation Electrodes. *Nano Lett.* **2017**, *17* (12), 7789−7795.
(41) Zhao, C.; Wang, Q.; Yao, Z.; Wang, J.; Sanchez-Lengeling, B.; Ding, F.; Qi, X.; Lu, Y.; Bai, X.; Li, B.; Li, H.; Aspuru-Guzik, A.; Huang, X.; Delmas, C.; Wagemaker, M.; Chen, L.; Hu, Y.-S. Rational design of layered oxide materials for sodium-ion batteries. *Science* **2020**, *370* (6517), 708−711.
(42) Yoon, C. S.; Jun, D.-W.; Myung, S.-T.; Sun, Y.-K. Structural Stability of $LiNiO_2$ Cycled above 4.2 V. *ACS Energy Lett.* **2017**, *2* (5), 1150−1155.
(43) Pouillerie, C.; Croguennec, L.; Delmas, C. The $Li_xNi_{1-y}Mg_yO_2$ (y = 0.05, 0.10) system: structural modifications observed upon cycling. *Solid State Ionics* **2000**, *132* (1), 15−29.
(44) Mortemard de Boisse, B.; Carlier, D.; Guignard, M.; Bourgeois, L.; Delmas, C. P2-$Na_xMn_{1/2}Fe_{1/2}O_2$ Phase Used as Positive Electrode in Na Batteries: Structural Changes Induced by the Electrochemical (De)intercalation Process. *Inorg. Chem.* **2014**, *53* (20), 11197−11205.
(45) Xu, C.; Märker, K.; Lee, J.; Mahadevegowda, A.; Reeves, P. J.; Day, S. J.; Groh, M. F.; Emge, S. P.; Ducati, C.; Layla Mehdi, B.; Tang, C. C.; Grey, C. P. Bulk fatigue induced by surface reconstruction in layered Ni-rich cathodes for Li-ion batteries. *Nat. Mater.* **2021**, *20* (1), 84−92.
(46) Lin, F.; Markus, I. M.; Nordlund, D.; Weng, T.-C.; Asta, M. D.; Xin, H. L.; Doeff, M. M. Surface reconstruction and chemical evolution of stoichiometric layered cathode materials for lithium-ion batteries. *Nat. Commun.* **2014**, *5* (1), 3529.
(47) Kasnatscheew, J.; Evertz, M.; Streipert, B.; Wagner, R.; Klöpsch, R.; Vortmann, B.; Hahn, H.; Nowak, S.; Amereller, M.; Gentschev, A. C.; Lamp, P.; Winter, M. The truth about the 1st cycle Coulombic efficiency of $LiNi_{1/3}Co_{1/3}Mn_{1/3}O_2$ (NCM) cathodes. *Phys. Chem. Chem. Phys.* **2016**, *18* (5), 3956−3965.
(48) Kasnatscheew, J.; Evertz, M.; Kloepsch, R.; Streipert, B.; Wagner, R.; CekicLaskovic, I.; Winter, M. Learning from Electrochemical Data:Simple Evaluation and Classification of LiMO2 _type-basedPositive Electrodes for Li -IonBatteries. *Energy Technology* **2017**, *5* (9), 1670−1679.
(49) Huang, J.; Zhong, L.; Wang, C.; Sullivan, J. P.; Xu, w.; Zhang, L.; Mao, S. X.; Hudak, N. S.; Liu, X.; Subramanian, A.; Fan, H.; Qi, L.; Kushima, A.; Li, J. In Situ Observation of the Electrochemical Lithiation of a Single SnO_2 Nanowire Electrode. *Science* **2010**, *330*, 1515−1520.
(50) Liu, X. H.; Zhong, L.; Huang, S.; Mao, S. X.; Zhu, T.; Huang, J. Y. Size-Dependent Fracture of Silicon Nanoparticles During Lithiation. *ACS Nano* **2012**, *6* (2), 1522−1531.
(51) Hess, J. B.; Barrett, C. S. Structure and nature of kink bands in zinc. *JOM* **1949**, *1* (9), 599−606.

https://doi.org/10.1021/acsenergylett.1c01976
ACS Energy Lett. 2021, 6, 3960−3969

(52) Kaufman, J. L.; Vinckevičiūtė, J.; Krishna Kolli, S.; Gabriel Goiri, J.; Van der Ven, A. Understanding intercalation compounds for sodium-ion batteries and beyond. *Philos. Trans. R. Soc., A* **2019**, *377* (2152), 20190020.
(53) Tapasztó, L.; Dumitrică, T.; Kim, S. J.; Nemes-Incze, P.; Hwang, C.; Biró, L. P. Breakdown of continuum mechanics for nanometre-wavelength rippling of graphene. *Nat. Phys.* **2012**, *8* (10), 739−742.
(54) Falin, A.; Cai, Q.; Santos, E. J. G.; Scullion, D.; Qian, D.; Zhang, R.; Yang, Z.; Huang, S.; Watanabe, K.; Taniguchi, T.; Barnett, M. R.; Chen, Y.; Ruoff, R. S.; Li, L. H. Mechanical properties of atomically thin boron nitride and the role of interlayer interactions. *Nat. Commun.* **2017**, *8* (1), 15815.

https://doi.org/10.1021/acsenergylett.1c01976
ACS Energy Lett. 2021, 6, 3960−3969